CHEMISTRY OF MATERIALS

pubs.acs.org/cm Article

$RuAl_6$—An Endohedral Aluminide Superconductor

Zuzanna Ryżyńska, Juan R. Chamorro, Tyrel M. McQueen, Piotr Wiśniewski, Dariusz Kaczorowski, Weiwei Xie, Robert J. Cava, Tomasz Klimczuk, and Michał J. Winiarski*

Cite This: *Chem. Mater.* 2020, 32, 3805−3812 Read Online

ACCESS | Metrics & More | Article Recommendations | Supporting Information

ABSTRACT: Superconductivity is reported in an endohedral aluminide compound, $RuAl_6$, with T_c = 1.21 K. The normalized heat capacity jump at T_c, $\Delta C/\gamma T_c$ = 1.58, confirms bulk superconductivity. The Ginzburg−Landau parameter of κ = 9.5 shows that $RuAl_6$ is a type-II superconductor. Electronic structure calculations for $RuAl_6$ are explored in comparison to its structural analogue $ReAl_6$ (T_c = 0.74 K). The stability of the phases is discussed in terms of the crystal orbital Hamilton population (−COHP) analysis. The difference in T_c in the two materials is caused by the significantly stronger electron−phonon coupling found in $RuAl_6$, which is a result of significantly stronger antibonding interactions. The presence of superconductivity in yet another compound made of aluminum clusters possibly expands the correlation of critical temperature and the structure shown for Ga-built clusters.

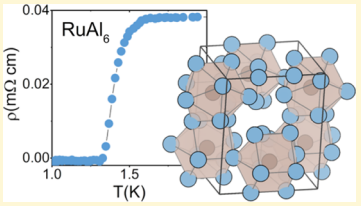

INTRODUCTION

One of the still unresolved problems of solid-state sciences is the design principle for superconductors, especially with high critical temperatures. The great effort to find universal relations that can be exploited to truly design superconducting materials led to a number of mostly empirical guidelines, such as the famous, semianecdotal Matthias rules.[1] Empirical relations between the superconducting critical temperature (T_c) and electron count per atom were also established in several groups of superconductors, including simple metallic elements,[2] A-15 compounds,[3] as well as Heusler[4] and high-entropy alloys.[5]

Recently, a group of gallium-rich intermetallic compounds, $ReGa_5$, Rh_2Ga_9, and Mo_8Ga_{41}, whose crystal structures are composed of interconnected endohedral Ga clusters, was found to be a host system for superconductivity with observed strong correlations between electron count, crystal structure, and superconducting critical temperature.[6] In this broad family of compounds, the crystal and electronic structures can be described by considering the whole basic cluster, instead of single atoms, as the main building block.[6]

Interestingly, while Rh_2Ga_9 and Ir_2Ga_9 are superconductors with T_c = 1.9 and 2.2 K, respectively,[7] the isoelectronic aluminides T_2Al_9 (T = Co, Rh, Ir) do not show superconductivity down to T = 2 K (see ref 8 and Figure S6 in the Supporting Information (SI)). It is also worth noting that a subtle difference between the crystal structures of T_2Ga_9 and T_2Al_9 phases exists, the former crystallizing in a noncentrosymmetric structure variant.[7,9] Aluminide analogues of the $ReGa_5$ and Mo_8Ga_{41} intermetallics are not known.

In this study, we report superconductivity in $RuAl_6$ with T_c = 1.21 K. The crystal structure of $RuAl_6$ (Figure 1), reported previously in 1968 by Edshammar,[10] can be described as a network of $RuAl_{10}$ polyhedra sharing edges along the c direction and corners along the a and b directions.

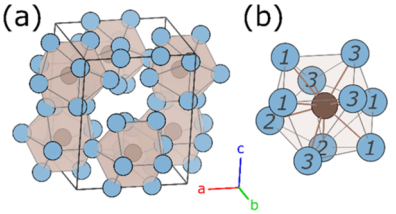

Figure 1. (a) Unit cell of $RuAl_6$: Ru atoms are shown in brown, Al in blue. $RuAl_{10}$ clusters share edges along the c direction and corners along the a and b directions. (b) $RuAl_{10}$ cluster with the three individual Al sites labeled.

The observation of the superconducting state in $RuAl_6$ supports the hypothesis of a high prevalence of superconductivity in the class of endohedral intermetallics. Along with the recently reported isostructural compound $ReAl_6$ (T_c = 0.74 K),[11,12] $RuAl_6$ forms one of the branches of the endohedral superconductor family.

Moreover, we observe a relationship between T_c and nearest-neighbor (NN) antibonding interactions in $ReAl_6$ and $RuAl_6$ and postulate that it is caused by their effects on the phonon structure, which in turn affects the electron−phonon coupling (EPC). We highlight that the relation between antibonding population (measured using the crystal orbital overlap population function, COHP) and super-

Received: December 20, 2019
Revised: April 15, 2020
Published: April 16, 2020

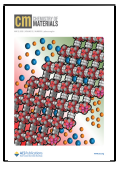

https://dx.doi.org/10.1021/acs.chemmater.9b05277
Chem. Mater. 2020, 32, 3805−3812

conductivity may be used as a simple guide for predicting superconductivity in new compounds.

MATERIALS AND METHODS

Polycrystalline samples of $RuAl_6$ were synthesized via an arc-melting method. Ru (Alfa Aesar, 99.95%) and Al pieces (Alfa Aesar, 99.99%) were put together on a water-cooled copper hearth with a Zr button used as an oxygen getter. The sample was turned and remelted several times to ensure homogeneity. Mass loss during synthesis was lower than 1%. The sample was then wrapped in thin tantalum foil, put in an evacuated quartz tube, and annealed at T = 620 °C (~40 °C below the melting point of Al and Al-rich eutectic[13]) for 14 days. After annealing, the ampoule was quenched in water at room temperature.

The powder X-ray diffraction (PXRD) pattern was collected at room temperature on a crushed sample with a Bruker D8 Focus diffractometer with Cu Kα radiation. FullProf software[14] was used for the Rietveld refinement of the $RuAl_6$ structure. The PXRD pattern of the annealed sample showed that a $RuAl_6$ phase was obtained with no observable amounts of impurity phases.

Single crystals of $RuAl_6$ were grown using a self-flux method.[15,16] Ru and Al pieces in a molar ratio of 3:97 were put in an alumina crucible, sealed in an evacuated quartz tube, heated to 1000 °C, slowly cooled to 670 °C, and subsequently centrifuged to remove the remaining Al flux. However, they were found to be contaminated with Al metal. Centrifugation above the melting point of Al (3000 rpm) and prolonged etching in a sodium hydroxide solution did not remove all of the elemental Al, which may be present in the form of inclusions within the crystals, as it was observed, e.g., in Al flux-grown SmB_6,[17] bulk Al shows a transition to the superconducting state at T_c = 1.2 K, overlapping with the T_c of $RuAl_6$. To avoid ambiguity, physical property measurements were performed only on a polycrystalline sample that was proven to be free of impurity phases, including Al (see Figures 2 and S2 in the Supporting Information).

Magnetization measurements were performed with a Quantum Design MPMS-XL SQUID magnetometer in a temperature range of T = 0.5−2.5 K and in a magnetic field of up to $\mu_0 H$ = 100 mT. Electrical resistivity was measured using a standard four-probe technique[18] with a Quantum Design Physical Property Measurement System (QD PPMS) in a temperature range of T = 0.4−300 K and in a magnetic field of up to $\mu_0 H$ = 350 mT, with temperatures T < 1.9 K reached using a ^{3}He evaporative cooling option.[19] A silver epoxy paste was used to attach platinum electrical contacts to the sample. Heat capacity measurements employing the standard semiadiabatic pulse technique[20,21] were done in the temperature range of 0.2−3 K using the ^{3}He−^{4}He dilution refrigerator option of the QD PPMS.[22−24]

To gain insight into the chemical bonding in $RuAl_6$ and the analogous $ReAl_6$ compound, calculations of the crystal orbital Hamilton population (−COHP)[25,26] were performed within the density functional theory (DFT) tight-binding linearized muffin-tin orbital atomic sphere approximation (TB−LMTO−ASA) as implemented in the Stuttgart code[27,28] employing the Perdew−Wang generalized gradient approximation (GGA) for the exchange-correlation potential.[29] Calculations were conducted using a 16 × 16 × 8 k-point mesh and experimental unit cells.

Detailed band structure and electronic density of states (DOS) calculations were performed by means of the DFT with the Perdew−Burke−Ernzerhof[30] GGA utilizing the ELK all-electron full-potential linearized augmented plane wave plus local orbitals code.[31] Calculations were conducted with spin−orbit coupling (SOC) using an 8 × 10 × 7 k-mesh.

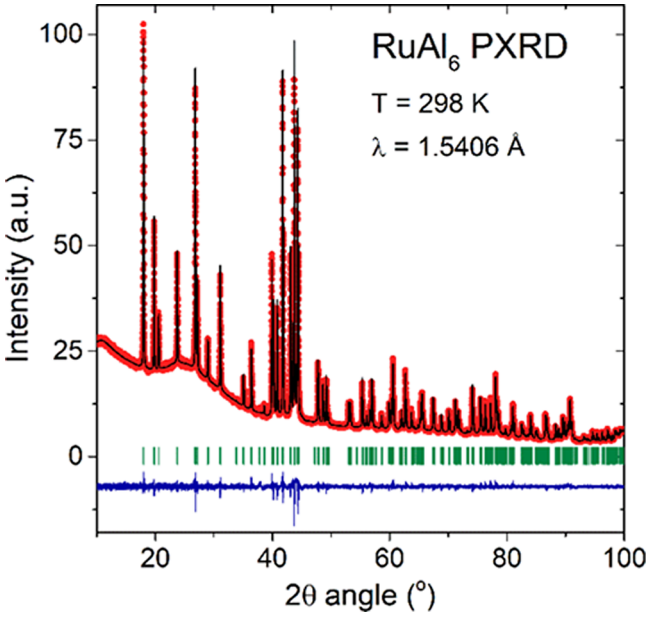

Figure 2. Rietveld fit (black line) to the room-temperature PXRD pattern (red dots) of $RuAl_6$. The blue line shows the difference between calculated and observed intensities. The green color marks the expected positions of Bragg reflections.

RESULTS AND DISCUSSION

The room-temperature powder X-ray diffraction pattern is presented in Figure 2. All of the Bragg peaks in the PXRD pattern are indexed with an orthorhombic *Cmcm* unit cell.

The lattice parameters and atomic positions obtained from the fit are in good agreement with those reported in the literature.[10] Table 1 presents the details of the $RuAl_6$ crystal structure derived from the Rietveld refinement.

Table 1. Crystallographic Data for $RuAl_6$ Obtained from the Rietveld Fit to the PXRD Pattern[a]

space group				*Cmcm* (# 63)
Pearson symbol				oS28
unit cell parameters (Å)				
a =				7.48502(1)
b =				6.55652(1)
c =				8.97105(1)
cell volume (Å^3)				440.402(1)
molar weight (g/mol)				262.96
number of formula units per cell—Z				4
density (calculated) (g/cm^3)				3.97
figures of merit				
R_p (%)				12.1
R_{wp} (%)				9.81
R_{exp} (%)				6.77
χ^2				2.10
atom	x	y	z	B (Å^2)
Al(1)	0.3196(1)	0	0	1.11(2)
Al(2)	0	0.1412(1)	0.1000(1)	1.62(2)
Al(3)	0.3207(1)	0.2942(1)	1/4	1.02(2)
Ru	0	0.4620(1)	1/4	0.44(1)

[a]Numbers given in parentheses are statistical uncertainties of the least significant digits. The R factors given are the conventional Rietveld R factors (background-corrected) calculated only for points with Bragg contributions.[32,33]

The zero-field-cooled (ZFC) and field-cooled (FC) dc magnetic susceptibilities are shown in Figure 3a. The onset of the transition to the superconducting state is visible in both ZFC and FC plots at T_c = 1.25 K. This temperature is defined as the temperature where the extrapolation of the steepest slope of $\chi(T)$ intersects the extrapolation of the normal state

https://dx.doi.org/10.1021/acs.chemmater.9b05277
Chem. Mater. 2020, 32, 3805−3812

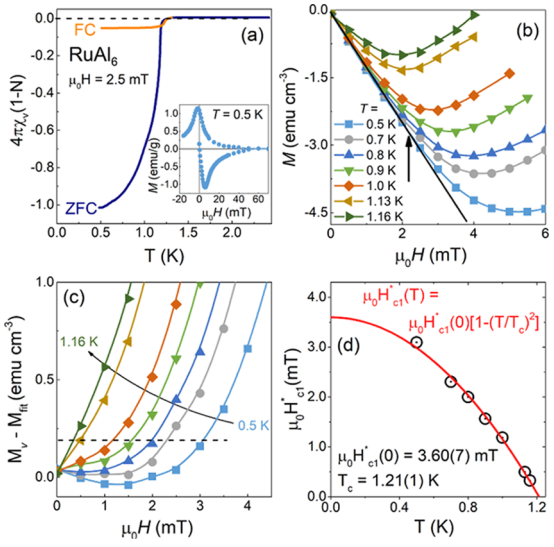

Figure 3. (a) Temperature-dependent ZFC and FC magnetization at an applied field of $\mu_0 H = 2.5$ mT, showing the transition to a perfectly diamagnetic Meissner state below $T = 1.25$ K. The volume susceptibility χ_V is corrected for the demagnetization factor derived from M_V vs H measurement (see (b,c)). Field-dependent magnetization below the T_c (inset to (a)) shows that $RuAl_6$ is a type-II superconductor. (b) Field-dependent magnetization curves measured at different temperatures below T_c. The black solid line is a linear fit in the low field limit. (c) Method of estimating the lower critical field, H_{c1}. (d) Lower critical field $H_{c1}^*(0)$ estimation.

susceptibility to lower temperatures.[34] After correction for the diamagnetic factor (discussed below), the magnitude of the saturated ZFC diamagnetic signal is close to the value of $-1/4\pi(1 - N)$ consistent with a full Meissner state (perfect diamagnetism), indicative of a complete transition to the superconducting state. The much smaller FC diamagnetic signal originates from the strong magnetic flux pinning present in the polycrystalline sample.

The volume magnetization vs magnetic field $M_v(H)$ plot measured at various temperatures below T_c is shown in the inset of Figure 3b. Assuming that a perfect diamagnet has a linear response to the magnetic field, the M_v vs H plot constructed at the lowest temperature (0.5 K) was fitted with a linear function ($M_{fit} = aH + b$). The value of the demagnetization factor (N) is then estimated using the equation $-a = \frac{1}{4\pi(1-N)}$ and is equal to $N = 0.33$. The demagnetization factor accounts for a sample shape-dependent distortion of the magnetic field inside and around a sample.[35] To plot the $(M_v - M_{fit})$ vs H graph in Figure 3c, the linear fit to the initial magnetization slope was constructed. The fields in which deviations from a linear response to the magnetic field are visible (marked with the black dashed line in Figure 3c) were taken as lower critical fields H_{c1}^*. The H_{c1}^* values derived for different temperatures were plotted vs temperature in Figure 3d and fitted with the equation $\mu_0 H_{c1}^*(T) = \mu_0 H_{c1}^*(0)[1 - (T/T_c)^2]$.[36] The value of critical field extrapolated to $T = 0$ K using the fitted function is $\mu_0 H_{c1}^*(0) = 3.60(7)$ mT. This value has to be corrected for the demagnetization factor, yielding $\mu_0 H_{c1}(0) = 5.4(1)$ mT. The critical temperature estimated from the fitting of the model to the data $T_c = 1.21(1)$ K is close to the value obtained from dc magnetization measurement. The full magnetization loop collected at a temperature of $T = 0.5$ K, below the superconducting transition, is shown in the inset of Figure 3a. The shape of the $M(H)$ loop suggests that $RuAl_6$ is a type-II superconductor.[36,37]

To further characterize the superconducting transition of $RuAl_6$, electrical resistivity measurements were performed in the temperature range of $T = 0.4$–300 K, presented in Figure 4a. At temperatures above T_c, $RuAl_6$ shows typical metallic

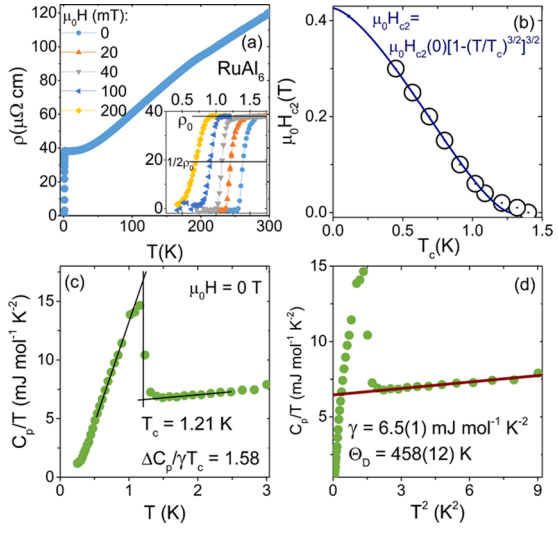

Figure 4. (a) Electrical resistivity of $RuAl_6$ at zero applied magnetic field, showing typical metallic behavior at high temperatures and a drop to zero below T_c; the inset shows the SC transition being suppressed by the applied magnetic field. (b) Dependence of the upper critical field H_{c2} on temperature. (c) Pronounced heat capacity anomaly at T_c, confirming the bulk nature of the SC transition; the electronic heat capacity coefficient γ and Debye temperature are shown.

behavior, with a residual resistivity ratio RRR = $\rho_{300}/\rho_0 \approx 4$, falling in the range typical for polycrystalline samples,[4,38,39] and residual resistivity $\rho_0 = 0.038$ mΩ cm.

The inset of Figure 4a presents the shift of superconducting transition toward lower temperatures with an applied magnetic field. The midpoints of the transitions gathered in this measurement were used to determine the upper critical shown in Figure 4b. The data were fitted with the formula proposed by Micnas et al.:[40] $\mu_0 H_{c2}(T) = \mu_0 H_{c2}(0)[1 - (T/T_c)^{3/2}]^{3/2}$ and gave the value $\mu_0 H_{c2}(0) = 426(7)$ mT, which will be used in further calculations.

Using the value of $\mu_0 H_{c2}(0)$ obtained from the fit and assuming that H_{c2} is purely due to orbital effects, the coherence length ξ_{GL} can be estimated from the equation $H_{c2}(0) = \phi_0/2\pi\xi_{GL}^2$ (where $\phi_0 = h/2e$ is the quantum of magnetic flux)[41,42] and is equal to $\xi_{GL} = 27.7(2)$ nm.

Heat capacity measurements on a $RuAl_6$ sample were performed to confirm the bulk nature of its superconductivity. Figure 4c shows the transition to the superconducting state of $RuAl_6$ without the applied magnetic field. A sharp anomaly confirms the bulk superconductivity. An equal-area entropy construction (solid black lines) was used to extract the transition temperature and the value of the specific heat jump. The superconducting critical temperature was determined to be $T_c = 1.21$ K, and the specific heat jump is $\Delta C_p/T = 10.3$ mJ mol^{-1} K^{-2}. Figure 4d shows the heat capacity of $RuAl_6$ as the C_p/T vs T^2 plot, fitted above the T_c using the formula of the low-temperature expansion of the Debye heat capacity model:

https://dx.doi.org/10.1021/acs.chemmater.9b05277
Chem. Mater. 2020, 32, 3805−3812

$C_p/T = \gamma + \beta T^2$, where γT and βT^3 are the electronic and phonon heat capacity contributions, respectively.[42] The fit yields $\gamma = 6.5(1)$ mJ mol^{-1} K^{-2} and $\beta = 0.14(1)$ mJ mol^{-1} K^{-4}. The Debye temperature is then calculated using β via the relation

$$\Theta_D = \sqrt[3]{\frac{12\pi^4 nR}{5\beta}}$$

where n is the number of atoms per formula unit ($n = 7$) and R is the gas constant. The resulting Debye temperature is Θ_D = 458(12) K. Taking the obtained γ, the normalized jump in specific heat equals $\Delta C/\gamma T_c = 1.58$, which is above the lower limit (1.43) predicted for weak coupling superconductors by the BCS theory, suggesting a bulk transition to the superconducting state.

To exclude the possibility that the superconducting transition is caused by an elemental Al impurity (T_c = 1.2 K), the heat capacity sample was ground after the measurement and a PXRD pattern was collected. The results (Figure S2 in the Supporting Information) show no observable amount of Al, confirming the bulk superconductivity of $RuAl_6$.

An alternative way of estimating the upper critical field of BCS superconductor is via the relation $H_c(0) = -AT_c \left.\frac{dH_c}{dT}\right|_{T=T_c}$, where A is a coefficient taking the value of 0.69 or 0.73 for the dirty or clean limit, respectively.[43] Taking T_c = 1.21 K and the slope of the $\mu_0 H_{c2}(T)$ data (Figure 4b) $d\mu_0 H_{c2}/dT = -0.426$ T/K, the calculation gives values of $\mu_0 H_{c2}$ = 360 and 380 mT for the dirty and clean limits, respectively.

The superconducting London penetration depth λ_{GL} can be estimated from the formula $H_{c1} = \frac{\phi_0}{4\pi\lambda_{GL}^2}\ln\frac{\lambda_{GL}}{\xi_{GL}}$. The estimated value of penetration depth for $RuAl_6$ is λ_{GL} = 265 nm. The Ginzburg–Landau parameter is calculated as $\kappa = \lambda_{GL}(0)/\xi_{GL}(0) = 9.5$. This value is significantly higher than $1/\sqrt{2}$, and the Ginzburg–Landau theory classifies $RuAl_6$ as a type-II superconductor, in contrast to type-I $ReAl_6$. The upper and lower critical fields can be linked to the thermodynamic critical field via the Ginzburg–Landau parameter: $H_{c1}H_{c2} = H_c^2 \ln\kappa$[44] and gives the value of $\mu_0 H_c$ = 32 mT.

All superconducting parameters are summarized in Table 2 and compared to results reported for $ReAl_6$ in ref 11.

The band structures and DOS of $RuAl_6$ and $ReAl_6$ are shown in Figure 5. DOS projections show that in both cases, the majority of DOS(E_F) is contributed by Al s and p orbitals, with the majority of Ru/Re d contribution lying well below the E_F. As shown in Figure S4 in the Supporting Information, the effects of SOC on the band structure of $RuAl_6$ were found to be negligible, while for $ReAl_6$, only minor differences were found between results calculated with and without SOC within 1 eV from the Fermi level. This is consistent with the fact that DOS around E_F is mostly contributed by Al s and p states. Since SOC has only negligible effects on the electronic structure, calculations of COHP using the scalar-relativistic TB–LMTO–ASA code can be considered reliable.

Surprisingly, the DOS(E_F) of both compounds was found to be very similar (<3% difference) even though T_c differs by a factor of ~1.6 and the γ electronic heat capacity coefficient is 30–40% lower in $ReAl_6$ than in $RuAl_6$. The value of γ is proportional to DOS(E_F) but is also renormalized by electron–phonon interactions: $\gamma = \gamma_{calc}(1 + \lambda_{el-ph})$, where

Table 2. Summary of Normal and Superconducting State Parameters for $RuAl_6$ Compared to $ReAl_6$. Unless Marked with Asterisk, Values for the Latter are Taken from ref 11

parameter	$RuAl_6$	$ReAl_6$
T_c (K)	1.21	0.74
$\mu_0 H_{c1}(0)$ (mT)	5.4(1)	
$\mu_0 H_{c2}(0)$ (mT)	426(7)	
$\mu_0 H_c(0)$ (mT)	32	44–50
ξ_{GL} (nm)	27.7	
λ_{GL} (nm)	265	
κ	9.5	
γ (mJ mol^{-1} K^{-2})	6.5(1)	3.9–4.7
Θ_D (K)	458(12)	~400
$\Delta C_{el}/\gamma T_c$	1.58	1.37–1.42
DOS(E_F) (states/eV/f.u.)	1.57	1.53*
γ_{calc} (mJ mol^{-1} K^{-2})	3.70	3.60*
λ_{el-ph}	0.81	0.08–0.31*

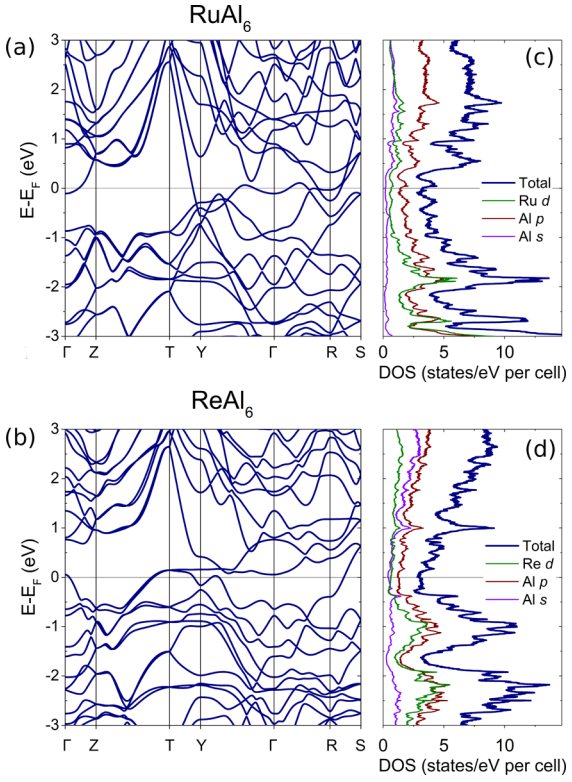

Figure 5. Band structure [(a), (c)] and density of states [(b), (d)] plots for $RuAl_6$ and $ReAl_6$ as obtained from the full-potential linearized augmented plane wave plus local orbital (FP-LAPW + LO) calculations. DOS in a wider energy range is shown in Figure S3 in the SI.

$\gamma_{calc} = \pi/3\ k_B^2 \cdot$DOS($E_F$) is the value obtained from DOS calculations and λ_{el-ph} is the dimensionless EPC coefficient.

One can estimate the value of the EPC coefficient via the relation $\lambda_{el-ph} = \frac{\gamma}{\gamma_{calc}} - 1$. This yields $\lambda_{el-ph} \approx 0.81$ for $RuAl_6$ and 0.08–0.31 for $ReAl_6$, suggesting that the difference in T_c in the two materials is caused by a significantly weaker EPC found in the latter.

In a simple form of the empirical McMillan formula,[45] T_c is linearly proportional to the Debye temperature

https://dx.doi.org/10.1021/acs.chemmater.9b05277
Chem. Mater. 2020, 32, 3805–3812

$$T_c = \frac{\Theta_D}{1.45} \exp\left(\frac{-1.04(1+\lambda_{el-ph})}{\lambda_{el-ph} - (1+0.62\lambda_{el-ph})\mu^*}\right)$$

where μ^* is the Coulomb pseudopotential parameter. Its value is equal to 0.1 in the case of nearly free electron metals and in cases the value of μ^* is assumed to be around 0.13; therefore, such a number is used for further estimations. The Θ_D value of $RuAl_6$ is only about 13% higher than that of $ReAl_6$ and cannot completely account for the increased T_c of the former. This suggests that the difference in T_c in the two materials is caused primarily by the difference in the EPC strengths, which in turn is affected strongly by the phonon spectrum.

The analysis of −COHP (Figure 6) shows that in $RuAl_6$, the peak in DOS near E_F derives from antibonding NN Ru−Al and

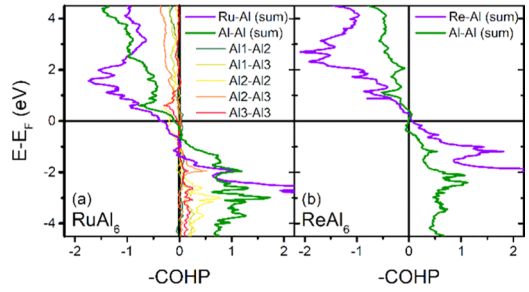

Figure 6. Crystal orbital Hamilton populations (−COHP) for $RuAl_6$ (a) and $ReAl_6$ (b) as obtained from TB−LMTO−ASA calculations.

Al−Al interactions (with the strongest contribution of Al_2−Al_2 in the latter case). The occupation of antibonding states is a driving force for instability toward either a crystal or electronic structure distortion. The latter may be manifested by an onset of itinerant ferromagnetism[46−48] or superconductivity.[49−53] In the case of $RuAl_6$, no structural transition is seen down to 2 K, as evidenced by heat capacity measurements (shown in Figure S1 in the Supporting Information) and thus, the electronic "strain" due to the antibonding electron population is reduced by opening a superconducting gap.

Out of all of the Al−Al pairs, the −COHP for Al_2−Al_2 shows the strongest antibonding interaction (Figure 6a). This results from the close contact between Al_2 atoms within the "void" and the $RuAl_{10}$ polyhedra seen in the [001] direction. Al_2 atoms form an infinite zigzag chain parallel to the c axis with alternating distances of d_1 = 2.58 and d_2= 2.69 Å. Such apparently empty space is also seen in the $PdGa_5$-type structure, in which it was found to be a region of high electron density due to intracluster bonding.[54]

Even though the unit cell parameters of $RuAl_6$ are smaller than those of $ReAl_6$, the Al_2−Al_2 distance is found to be shorter in the latter (d_1 = 2.57, d_2 = 2.65 Å). This highlights the effect of bond weakening by additional electrons occupying antibonding states.

In $ReAl_6$, the Re−Al states around E_F are of a bonding nature, but weak antibonding interactions between NN Al atoms are also observed. Since the DOS(E_F) of both compounds is almost the same, one can postulate that stronger antibonding interactions in $RuAl_6$ are, at least partially, responsible for the enhanced T_c through their influence on the EPC.

This suggests a way to further increase the T_c by electron doping $RuAl_6$ (partial Rh or Ir substitution for Ru)—while a small amount of dopant is expected to enhance T_c, a larger amount will inevitably result in the destabilization of the crystal structure. This is in agreement with the fact that no $MnAl_6$-type phase is known to exist in the Rh−Al system, the most Al-rich intermetal in the system being the endohedral cluster compound Rh_2Al_9.[55] COHP calculations for hypothetical "$RhAl_6$" show much stronger antibonding interactions (Figure 7a) and a DOS(E) peak (Figure 7b) near E_F, both in agreement with the instability of the structure.

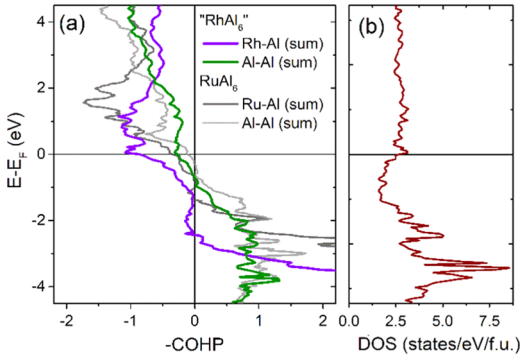

Figure 7. (a) COHP curves for a hypothetical $RhAl_6$ compound compared to $RuAl_6$. (b) DOS for $RhAl_6$ calculated within the TB−LMTO−ASA approximation showing a DOS peak near E_F.

The presence of antibonding population results in a decrease in the bond strength and thus phonon mode softening. Allen and Cohen[56] discussed the positive correlation between mode softening and increased superconducting T_c in rocksalt-type transition-metal carbides, such as HfC (T_c < 0.02 K) and TaC ($T_c \approx 11$ K). In HfC, the Fermi level lies in the Hf−C bonding region (see Supporting Information Figure S4 for −COHP curves) and the additional electrons in TaC populate antibonding orbitals, leading to the decrease in the bonding strength. In our system, the effect on T_c is more subtle, yet it is still the likely reason for the enhanced transition temperature of $RuAl_6$ compared to $ReAl_6$.

Figure 8 shows the $MnAl_6$-type crystal structure compared to other Al-rich binary phases of group 6−9 transition metals

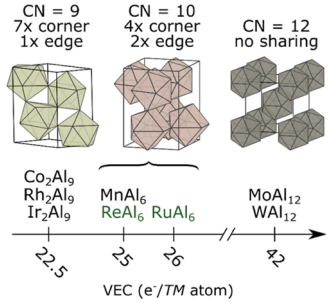

Figure 8. Comparison of the crystal structures of Al-rich intermetallic compounds of group 6−9 transition metals (TMs).

(TMs). In each case, the total valence electron count (VEC) per TM atom is higher than 18, which suggests that significant direct Al−Al bonding is present.[57−59] The decreasing coordination number of TM with increasing group number can be, at least partially, rationalized in terms of atomic contraction along the d series of the periodic table: a higher number of neighbors is expected around a larger atom. This phenomenon is also likely responsible for the lack of Ga

https://dx.doi.org/10.1021/acs.chemmater.9b05277
Chem. Mater. 2020, 32, 3805−3812

analogues of $ReAl_6$ and $RuAl_6$ as the atomic and covalent radii of Ga are larger than those of Al.[60,61]

CONCLUSIONS

We have studied the superconductivity of $RuAl_6$. Resistivity, magnetic susceptibility, and heat capacity measurements show superconducting behavior with T_c = 1.21 K. $RuAl_6$ with 26 electrons per transition metal places itself on the rightmost part of the T_c vs e^- per transition metal diagram of endohedral superconductors.[6] While there is recent evidence that the VEC-T_c behavior extends further to the low VEC region ($Re_8Ga_{19.8}Zn_{21.2}$ was reported to remain metallic at least down to T = 1.8 K[62]), the low-temperature (T < 2 K) physical properties of $PdGa_5$ (VEC = 25) and M_2Al_9 (M = Co, Rh, Ir) (VEC = 22.5) are not reported, and we cannot draw a conclusion whether $RuAl_6$ and, more generally, Al-based endohedral compounds family follow the trend observed for the gallide endohedral superconductors. An interesting question is whether the COHP analysis can explain the difference between isostructural V_8Ga_{41} (no SC transition down to 2 K) and Mo_8Ga_{41} (T_c = 9.8 K).[6] Unfortunately, due to very large unit cells (48 atoms in the primitive cell), we were not able to perform such calculations. Further investigation of Al-built endohedral cluster superconductors is needed to fully outline the appearance of the diagram for T_c of such compounds.

Interestingly, according to the Topological Materials Database and Materiae,[63−67] $RuAl_6$ is a candidate topological material, making it a possibly useful system to study the interplay between superconductivity and topology.

Superconductivity is often observed at the edge of a structural transition, such as a charge density wave distortion. A classic example is elemental tellurium, which crystallizes in a trigonal α-Se structure, which can be derived from the simple cubic α-Po structure via a Peierls distortion.[47] The distortion can be rationalized in terms of reduction of strong antibonding interactions present in the case of Te in the α-Po-type structure.[47] If, however, the distortion is suppressed by the application of high pressure, Te becomes metallic and shows superconductivity with $T_c \approx 7.5$ K.[68] Note that while the high-pressure structure of Te is body-centered cubic instead of simple cubic, the strong antibonding Te−Te interactions are still present.[69]

This competition between the structural distortion and superconductivity is observed in various other systems (e.g., $TiSe_2$[70]) and in general can be seen as stemming from two competing phenomena induced by the strong EPC: T_c is enhanced by an increase of EPC, but only to the point where a strong EPC destabilizes the original structure, resulting in more strongly bonded one with lower DOS(E_F) and suppressed T_c.

The correlation between T_c and the antibonding population, as observed in $RuAl_6$ and $ReAl_6$, can be used as a simple rule that helps to search for superconductor candidates. In fact, a correlation between antibonding population and superconductivity has been reported for other, chemically distinct systems: NbRuB[52] and SrSnP,[53] for example, and also, e.g., in $ThCr_2Si_2$-type KNi_2S_2 and KNi_2Se_2 compounds.[49−51] This criterion is useful for the initial screening of superconductor candidates, as it is based only on the crystal structure and the results of relatively simple electronic structural calculations and does not require computationally demanding phonon structure calculations.

ASSOCIATED CONTENT

Supporting Information

The Supporting Information is available free of charge at https://pubs.acs.org/doi/10.1021/acs.chemmater.9b05277.

Heat capacity of $RuAl_6$ at T = 2−300 K; XRD pattern of the $RuAl_6$ sample used for heat capacity measurements; electronic band structures and DOS for $RuAl_6$ and $ReAl_6$ in a wider energy range; −COHP curves for HfC and TaC; and resistivity of M_2Al_9 (M = Co, Rh, Ir) (PDF)

AUTHOR INFORMATION

Corresponding Author

Michał J. Winiarski − *Faculty of Applied Physics and Mathematics and Advanced Materials Center, Gdansk University of Technology, 80-233 Gdansk, Poland; Department of Chemistry, Department of Physics and Astronomy, and Institute for Quantum Matter, Johns Hopkins University, Baltimore, Maryland 21218, United States;* orcid.org/0000-0001-9083-8066; Email: michal.winiarski@pg.edu.pl

Authors

Zuzanna Ryżyńska − *Faculty of Applied Physics and Mathematics and Advanced Materials Center, Gdansk University of Technology, 80-233 Gdansk, Poland*

Juan R. Chamorro − *Department of Chemistry, Department of Physics and Astronomy, and Institute for Quantum Matter, Johns Hopkins University, Baltimore, Maryland 21218, United States;* orcid.org/0000-0002-0462-5580

Tyrel M. McQueen − *Department of Chemistry, Department of Physics and Astronomy, and Institute for Quantum Matter and Department of Materials Science and Engineering, Johns Hopkins University, Baltimore, Maryland 21218, United States;* orcid.org/0000-0002-8493-4630

Piotr Wiśniewski − *Institute of Low Temperature and Structure Research, Polish Academy of Sciences, 50-950 Wrocław, Poland*

Dariusz Kaczorowski − *Institute of Low Temperature and Structure Research, Polish Academy of Sciences, 50-950 Wrocław, Poland*

Weiwei Xie − *Department of Chemistry, Louisiana State University, Baton Rouge, Louisiana 70803, United States;* orcid.org/0000-0002-5500-8195

Robert J. Cava − *Department of Chemistry, Princeton University, Princeton, New Jersey 08544, United States*

Tomasz Klimczuk − *Faculty of Applied Physics and Mathematics and Advanced Materials Center, Gdansk University of Technology, 80-233 Gdansk, Poland;* orcid.org/0000-0002-7089-4631

Complete contact information is available at: https://pubs.acs.org/10.1021/acs.chemmater.9b05277

Author Contributions

This manuscript was written through thorough contributions of all authors.

Notes

The authors declare no competing financial interest.

ACKNOWLEDGMENTS

This work was supported as part of the Institute for the Quantum Matter, an Energy Frontier Research Center funded by the US Department of Energy, Office of Science, Office of Basic Energy Sciences, under award DE-SC0019331. The research performed at the Gdansk University of Technology

was supported by the National Science Centre (Poland) grant (UMO-2016/22/M/ST5/00435). The work at Princeton University was funded by the US DOE Division of Basic Energy Sciences, grant DE-FG02-ER45706. J.R.C. acknowledges the Gompf Family Fellowship for support. T.M.M. acknowledges support of the David and Lucile Packard Foundation. M.J.W. was supported by the Foundation for Polish Science (FNP).

■ ABBREVIATIONS

COHP, crystal orbital Hamilton population; DOS, density of states; EPC, electron−phonon coupling; FC, field cooling; NN, nearest neighbors; XRD, X-ray diffraction; ZFC, zero-field cooling

■ REFERENCES

(1) Conder, K. A Second Life of the Matthias's Rules. *Supercond. Sci. Technol.* **2016**, *29*, No. 080502.
(2) Matthias, B. T. The Search for High-temperature Superconductors. *Phys. Today* **1971**, *24*, 23.
(3) Matthias, B. T. Transition Temperatures of Superconductors. *Phys. Rev.* **1953**, *92*, 874−876.
(4) Klimczuk, T.; Wang, C. H.; Gofryk, K.; Ronning, F.; Winterlik, J.; Fecher, G. H.; Griveau, J.-C.; Colineau, E.; Felser, C.; Thompson, J. D.; Safarik, D. J.; Cava, R. J. Superconductivity in the Heusler Family of Intermetallics. *Phys. Rev. B* **2012**, *85*, No. 174505.
(5) von Rohr, F.; Winiarski, M. J.; Tao, J.; Klimczuk, T.; Cava, R. J. Effect of Electron Count and Chemical Complexity in the Ta-Nb-Hf-Zr-Ti High-Entropy Alloy Superconductor. *Proc. Natl. Acad. Sci. U.S.A.* **2016**, *113*, E7144−E7150.
(6) Xie, W.; Luo, H.; Phelan, B. F.; Klimczuk, T.; Cevallos, F. A.; Cava, R. J. Endohedral Gallide Cluster Superconductors and Superconductivity in ReGa5. *Proc. Natl. Acad. Sci. U.S.A.* **2015**, *112*, E7048−E7054.
(7) Shibayama, T.; Nohara, M.; Katori, H. A.; Okamoto, Y.; Hiroi, Z.; Takagi, H. Superconductivity in Rh2Ga9 and Ir2Ga9 without Inversion Symmetry. *J. Phys. Soc. Jpn.* **2007**, *76*, 073708.
(8) Caplin, A. D.; Grüner, G.; Dunlop, J. B. Al10V: An Einstein Solid. *Phys. Rev. Lett.* **1973**, *30*, 1138−1140.
(9) Boström, M.; Rosner, H.; Prots, Y.; Burkhardt, U.; Grin, Y. The Co2Al9 Structure Type Revisited. *Z. Anorg. Allg. Chem.* **2005**, *631*, 534−541.
(10) Edshammar, L.-E. The Crystal Structure of RuAl6. *Acta Chem. Scand.* **1968**, *22*, 2374−2375.
(11) Peets, D. C.; Cheng, E.; Ying, T.; Kriener, M.; Shen, X.; Li, S.; Feng, D. Type-I Superconductivity in Al6Re. *Phys. Rev. B* **2019**, *99*, No. 144519.
(12) Cheng, E.; Peets, D. C.; Xi, C.; Huang, Y.; Pi, L.; Li, S. Magnetotransport in Al6Re. *Phys. Rev. B* **2019**, *100*, No. 054509.
(13) Mi, S.; Balanetskyy, S.; Grushko, B. A Study of the Al-Rich Part of the Al−Ru Alloy System. *Intermetallics* **2003**, *11*, 643−649.
(14) Rodríguez-Carvajal, J. Recent Advances in Magnetic Structure Determination by Neutron Powder Diffraction. *Phys. B* **1993**, *192*, 55−69.
(15) Canfield, P. C.; Fisk, Z. Growth of Single Crystals from Metallic Fluxes. *Philos. Mag. B* **1992**, *65*, 1117−1123.
(16) Kanatzidis, M. G.; Pöttgen, R.; Jeitschko, W. The Metal Flux: A Preparative Tool for the Exploration of Intermetallic Compounds. *Angew. Chem., Int. Ed.* **2005**, *44*, 6996−7023.
(17) Phelan, W. A.; Koohpayeh, S. M.; Cottingham, P.; Tutmaher, J. A.; Leiner, J. C.; Lumsden, M. D.; Lavelle, C. M.; Wang, X. P.; Hoffmann, C.; Siegler, M. A.; Haldolaarachchige, N.; Young, D. P.; McQueen, T. M. On the Chemistry and Physical Properties of Flux and Floating Zone Grown SmB 6 Single Crystals. *Sci. Rep.* **2016**, *6*, No. 20860.
(18) Miccoli, I.; Edler, F.; Pfnür, H.; Tegenkamp, C. The 100th Anniversary of the Four-Point Probe Technique: The Role of Probe Geometries in Isotropic and Anisotropic Systems. *J. Phys.: Condens. Matter* **2015**, *27*, No. 223201.
(19) Physical Property Measurement System Helium-3 RefrigeratorSystem User's Manual, 1092-100, Rev. D7. Quantum Design July, 2017.
(20) Hwang, J. S.; Lin, K. J.; Tien, C. Measurement of Heat Capacity by Fitting the Whole Temperature Response of a Heat-Pulse Calorimeter. *Rev. Sci. Instrum.* **1997**, *68*, 94−101.
(21) Physical Property Measurement System Heat Capacity OptionUser's Manual, 1085-150, Rev. M6. Quantum Design February, 2015.
(22) Radebaugh, R.; Siegwarth, J. D. Dilution Refrigerator Technology. *Cryogenics* **1971**, *11*, 368−384.
(23) Das, P.; de Ouboter, R. B.; Taconis, K. W. A Realization of a London-Clarke-Mendoza Type Refrigerator. In *Low Temperature Physics LT9*; Daunt, J. G.; Edwards, D. O.; Milford, F. J.; Yaqub, M., Eds.; Springer: Boston, MA, 1965; pp 1253−1255.
(24) Physical Property Measurement System Dilution Refrigerator-User's Manual, 1091-100, Rev. A5. Quantum Design January, 2013.
(25) Dronskowski, R.; Bloechl, P. E. Crystal Orbital Hamilton Populations (COHP): Energy-Resolved Visualization of Chemical Bonding in Solids Based on Density-Functional Calculations. *J. Phys. Chem. A* **1993**, *97*, 8617−8624.
(26) Steinberg, S.; Dronskowski, R. The Crystal Orbital Hamilton Population (COHP) Method as a Tool to Visualize and Analyze Chemical Bonding in Intermetallic Compounds. *Crystals* **2018**, *8*, No. 225.
(27) The STUTTGART TB-LMTO-ASA program. https://www2.fkf.mpg.de/andersen/LMTODOC/LMTODOC.html (accessed April 15, 2020).
(28) Skriver, H. L. *The LMTO Method: Muffin-Tin Orbitals and Electronic Structure*; Springer-Verlag: Berlin; New York, 1984.
(29) Perdew, J. P.; Wang, Y. Accurate and Simple Analytic Representation of the Electron-Gas Correlation Energy. *Phys. Rev. B* **1992**, *45*, 13244−13249.
(30) Perdew, J. P.; Burke, K.; Ernzerhof, M. Generalized Gradient Approximation Made Simple. *Phys. Rev. Lett.* **1996**, *77*, 3865−3868.
(31) The Elk Code. http://elk.sourceforge.net (accessed April 15, 2020).
(32) Toby, B. H. R. Factors in Rietveld Analysis: How Good Is Good Enough? *Powder Diffr.* **2006**, *21*, 67−70.
(33) Huot, J.; Černý, R. Neutron Powder Diffraction. In Neutron Scattering and Other Nuclear Techniques for Hydrogen in Materials. In *Neutron Scattering Applications and Techniques*; Fritzsche, H.; Huot, J.; Fruchart, D., Eds.; Springer International Publishing, 2016; pp 31−89.
(34) Klimczuk, T.; Cava, R. J. Carbon Isotope Effect in Superconducting MgCNi3. *Phys. Rev. B* **2004**, *70*, No. 212514.
(35) Prozorov, R.; Kogan, V. G. Effective Demagnetizing Factors of Diamagnetic Samples of Various Shapes. *Phys. Rev. Appl.* **2018**, *10*, No. 014030.
(36) Powell, R. L.; Clark, A. F. Definitions of Terms for Practical Superconductors. 2. Critical Parameters. *Cryogenics* **1978**, *18*, 137−141.
(37) Fickett, F. R. Standards for Measurement of the Critical Fields of Superconductors. *J. Res. Natl. Bur. Stand.* **1985**, *90*, 95−113.
(38) Klimczuk, T.; Szlawska, M.; Kaczorowski, D.; O'Brien, J. R.; Safarik, D. J. Superconductivity in the Einstein Solid V Al 10.1. *J. Phys.: Condens. Matter* **2012**, *24*, No. 365701.
(39) Winiarski, M. J.; Wiendlocha, B.; Sternik, M.; Wiśniewski, P.; O'Brien, J. R.; Kaczorowski, D.; Klimczuk, T. Rattling-Enhanced Superconductivity in MV2Al20 (M=Sc, Lu, Y) Intermetallic Cage Compounds. *Phys. Rev. B* **2016**, *93*, No. 134507.
(40) Micnas, R.; Ranninger, J.; Robaszkiewicz, S. Superconductivity in Narrow-Band Systems with Local Nonretarded Attractive Interactions. *Rev. Mod. Phys.* **1990**, *62*, 113−171.
(41) Tinkham, M. *Introduction to Superconductivity*; McGraw Hill: New York, 1996.

https://dx.doi.org/10.1021/acs.chemmater.9b05277
Chem. Mater. 2020, 32, 3805−3812

(42) Charles, K. *Introduction to Solid State Physics*, 8th ed.; Wiley: Hoboken, 2004.
(43) Werthamer, N. R.; Helfand, E.; Hohenberg, P. C. Temperature and Purity Dependence of the Superconducting Critical Field, Hc2. III. Electron Spin and Spin-Orbit Effects. *Phys. Rev.* **1966**, *147*, 295−302.
(44) Cyrot, M.; Pavuna, D.*Introduction to Superconductivity and High-Tc Materials*; World Scientific, 1992.
(45) McMillan, W. L. Transition Temperature of Strong-Coupled Superconductors. *Phys. Rev.* **1968**, *167*, 331−344.
(46) Dronskowski, R.; Korczak, K.; Lueken, H.; Jung, W. Chemically Tuning between Ferromagnetism and Antiferromagnetism by Combining Theory and Synthesis in Iron/Manganese Rhodium Borides. *Angew. Chem., Int. Ed.* **2002**, *41*, 2528−2532.
(47) Decker, A.; Landrum, G. A.; Dronskowski, R. Structural and Electronic Peierls Distortions in the Elements (A): The Crystal Structure of Tellurium. *Z. Anorg. Allg. Chem.* **2002**, *628*, 295−302.
(48) Fokwa, B. P. T.; Lueken, H.; Dronskowski, R. Rational Synthetic Tuning between Itinerant Antiferromagnetism and Ferromagnetism in the Complex Boride Series Sc2FeRu5−nRhnB2 (0≤n≤5). *Chem. - Eur. J.* **2007**, *13*, 6040−6046.
(49) Neilson, J. R.; McQueen, T. M. Bonding, Ion Mobility, and Rate-Limiting Steps in Deintercalation Reactions with ThCr2Si2-Type KNi2Se2. *J. Am. Chem. Soc.* **2012**, *134*, 7750−7757.
(50) Neilson, J. R.; Llobet, A.; Stier, A. V.; Wu, L.; Wen, J.; Tao, J.; Zhu, Y.; Tesanovic, Z. B.; Armitage, N. P.; McQueen, T. M. Mixed-Valence-Driven Heavy-Fermion Behavior and Superconductivity in KNi2Se2. *Phys. Rev. B* **2012**, *86*, No. 054512.
(51) Neilson, J. R.; McQueen, T. M.; Llobet, A.; Wen, J.; Suchomel, M. R. Charge Density Wave Fluctuations, Heavy Electrons, and Superconductivity in KNi2S2. *Phys. Rev. B* **2013**, *87*, No. 045124.
(52) Xie, W.; Luo, H.; Baroudi, K.; Krizan, J. W.; Phelan, B. F.; Cava, R. J. Fragment-Based Design of NbRuB as a New Metal-Rich Boride Superconductor. *Chem. Mater.* **2015**, *27*, 1149−1152.
(53) Gui, X.; Sobczak, Z.; Chang, T.-R.; Xu, X.; Huang, A.; Jia, S.; Jeng, H.-T.; Klimczuk, T.; Xie, W. Superconducting SrSnP with Strong Sn−P Antibonding Interaction: Is the Sn Atom Single or Mixed Valent? *Chem. Mater.* **2018**, *30*, 6005−6013.
(54) Grin, Y.; Wedig, U.; Wagner, F.; von Schnering, H. G.; Savin, A. The Analysis of "Empty Space" in the PdGa5 Structure. *J. Alloys Compd.* **1997**, *255*, 203−208.
(55) Okamoto, H. Al-Rh (Aluminum-Rhodium). *J. Phase Equilib. Diffus.* **2007**, *28*, 485.
(56) Allen, P. B.; Cohen, M. L. Superconductivity and Phonon Softening. *Phys. Rev. Lett.* **1972**, *29*, 1593−1596.
(57) Yannello, V. J.; Fredrickson, D. C. Orbital Origins of Helices and Magic Electron Counts in the Nowotny Chimney Ladders: The 18 − n Rule and a Path to Incommensurability. *Inorg. Chem.* **2014**, *53*, 10627−10631.
(58) Yannello, V. J.; Fredrickson, D. C. Generality of the 18-n Rule: Intermetallic Structural Chemistry Explained through Isolobal Analogies to Transition Metal Complexes. *Inorg. Chem.* **2015**, *54*, 11385−11398.
(59) Miyazaki, K.; Yannello, V. J.; Fredrickson, D. C. Electron-Counting in Intermetallics Made Easy: The 18-n Rule and Isolobal Bonds across the Os−Al System. *Z. Kristallogr. - Cryst. Mater.* **2017**, *232*, 487−496.
(60) Slater, J. C. Atomic Radii in Crystals. *J. Chem. Phys.* **1964**, *41*, 3199−3204.
(61) Cordero, B.; Gómez, V.; Platero-Prats, A. E.; Revés, M.; Echeverría, J.; Cremades, E.; Barragán, F.; Alvarez, S. Covalent Radii Revisited. *Dalton Trans.* **2008**, *21*, 2832−2838.
(62) Verchenko, V. Y.; Mironov, A. V.; Wei, Z.; Tsirlin, A. A.; Dikarev, E. V.; Shevelkov, A. V. Crystal Growth of Intermetallics from the Joint Flux: Exploratory Synthesis through the Control of Valence Electron Count. *Inorg. Chem.* **2019**, *58*, 1561−1570.
(63) Bradlyn, B.; Elcoro, L.; Cano, J.; Vergniory, M. G.; Wang, Z.; Felser, C.; Aroyo, M. I.; Bernevig, B. A. Topological Quantum Chemistry. *Nature* **2017**, *547*, 298−305.
(64) Vergniory, M. G.; Elcoro, L.; Felser, C.; Regnault, N.; Bernevig, B. A.; Wang, Z. A Complete Catalogue of High-Quality Topological Materials. *Nature* **2019**, *566*, 480−485.
(65) Topological Materials Database. https://www.topologicalquantumchemistry.org/#/detail/58157 (accessed April 15, 2020).
(66) Zhang, T.; Jiang, Y.; Song, Z.; Huang, H.; He, Y.; Fang, Z.; Weng, H.; Fang, C. Catalogue of Topological Electronic Materials. *Nature* **2019**, *566*, 475−479.
(67) Topological properties and more for material Al6Ru (sg63)| Materiae. http://materiae.iphy.ac.cn/materials/MAT00012610 (accessed April 15, 2020).
(68) Simon, A. Superconductivity and the Periodic Table: From Elements to Materials. *Philos. Trans. R. Soc., A* **2015**, *373*, No. 20140192.
(69) Mauri, F.; Zakharov, O.; de Gironcoli, S.; Louie, S. G.; Cohen, M. L. Phonon Softening and Superconductivity in Tellurium under Pressure. *Phys. Rev. Lett.* **1996**, *77*, 1151−1154.
(70) Kusmartseva, A. F.; Sipos, B.; Berger, H.; Forró, L.; Tutiš, E. Pressure Induced Superconductivity in Pristine 1T-TiSe2. *Phys. Rev. Lett.* **2009**, *103*, No. 236401.

https://dx.doi.org/10.1021/acs.chemmater.9b05277
Chem. Mater. 2020, 32, 3805−3812